Subdiffraction light focusing using a cross sectional ridge waveguide nanoscale aperture

LUIS TRAVERSO, ANURUP DATTA, AND XIANFAN XU*

School of Mechanical Engineering and Birck Nanotechnology Center, Purdue University, West Lafayette, IN 47906, USA
*xxu@ecn.purdue.edu

Abstract: We report a new type of plasmonic nanoscale ridge aperture and its fabrication process which is based on layer-by-layer planar lithography. This new fabrication method allows us to create desired nanoscale features of a plasmonic ridge waveguide nanoscale aperture, which helps to confine a near-field spot to sub-wavelength dimensions. Numerical simulations using Finite Element Method (FEM) are performed to calculate the near-field distribution around the exit of the aperture. Measurements using scattering near-field scanning optical microscopy (s-NSOM) confirm the design and demonstrate that the aperture is capable of producing focused spots in the ridge gap at the exit of the aperture. The planar lithography process is a step toward mass production of such plasmonic structures for applications including heat-assisted magnetic recording (HAMR).

References and links

1. S. A. Maier, *Plasmonics: Fundamentals and Applications* (Springer, 2007).
2. S. Hayashi and T. Okamoto, "Plasmonics: visit the past to know the future," J. Phys. D Appl. Phys. **45**(43), 433001 (2012).
3. D. R. Mason, S. G. Menabde, S. Yu, and N. Park, "Plasmonic excitations of 1D metal-dielectric interfaces in 2D systems: 1D surface plasmon polaritons," Sci. Rep. **4**, 4536 (2014).
4. J. Zhang and L. Zhang, "Nanostructures for surface plasmons," Adv. Opt. Photonics **4**(2), 157–321 (2012).
5. M.-K. Kim, H. Sim, S. J. Yoon, S.-H. Gong, C. W. Ahn, Y.-H. Cho, and Y.-H. Lee, "Squeezing photons into a point-like space," Nano Lett. **15**(6), 4102–4107 (2015).
6. Y. Wang, Z. Du, Y. Park, C. Chen, X. Zhang, and L. Pan, "Quasi-3D plasmonic coupling scheme for near-field optical lithography and imaging," Opt. Lett. **40**(16), 3918–3921 (2015).
7. P. Bharadwaj, B. Deutsch, and L. Novotny, "Optical antennas," Adv. Opt. Photonics **1**(3), 438–483 (2009).
8. Z. Xie, W. Yu, T. Wang, H. Zhang, Y. Fu, H. Liu, F. Li, Z. Lu, and Q. Sun, "Plasmonic nanolithography: A review," Plasmonics **6**(30), 565–580 (2011).
9. X. Shi and L. Hesselink, "Mechanisms for enhancing power throughput from planar nano-apertures for near field optical data storage," Jpn. J. Appl. Phys. **41**(1), 1632–1635 (2002).
10. K. Şendur, W. Challener, and C. Peng, "Ridge waveguide as a near field aperture for high density data storage," J. Appl. Phys. **96**(5), 2743–2752 (2004).
11. N. Murphy-DuBay, L. Wang, E. C. Kinzel, S. M. V. Uppuluri, and X. Xu, "Nanopatterning using NSOM probes integrated with high transmission nanoscale bowtie aperture," Opt. Express **16**(4), 2584–2589 (2008).
12. S. M. Uppuluri, E. C. Kinzel, Y. Li, and X. Xu, "Parallel optical nanolithography using nanoscale bowtie aperture array," Opt. Express **18**(7), 7369–7375 (2010).
13. X. Wen, A. Datta, L. M. Traverso, L. Pan, X. Xu, and E. E. Moon, "High throughput optical lithography by scanning a massive array of bowtie aperture antennas at near-field," Sci. Rep. **5**, 16192 (2015).
14. N. Zhou, X. Xu, A. T. Hammack, B. C. Stipe, K. Gao, W. Scholz, and E. C. Gage, "Plasmonic near-field transducer for heat-assisted magnetic recording," Nanophotonics **3**(3), 141–155 (2014).
15. M. H. Kryder, E. C. Gage, T. W. McDaniel, W. A. Challener, R. E. Rottmayer, Ganping Ju, Yiao-Tee Hsia, and M. F. Erden, "Heat assisted magnetic recording," Proc. IEEE **96**(11), 1810–1835 (2008).
16. M. P. Sharrock, "Time-dependent magnetic phenomena and particle-size effects in recording media," IEEE Trans. Magn. **26**(1), 193–197 (1990).
17. W. A. Challener, C. Peng, A. V. Itagi, D. Karns, W. Peng, Y. Peng, X. Yang, X. Zhu, N. J. Gokemeijer, Y. T. Hsia, G. Ju, R. E. Rottmayer, M. A. Seigler, and E. C. Gage, "Heat-assisted magnetic recording by a near-field transducer with efficient optical energy transfer," Nat. Photonics **3**(4), 220–224 (2009).

18. B. C. Stipe, T. C. Strand, C. C. Poon, H. Balamane, T. D. Boone, J. A. Katine, J.-L. Li, V. Rawat, H. Nemoto, A. Hirotsune, O. Hellwig, R. Ruiz, E. Dobisz, D. S. Kercher, N. Robertson, T. R. Albrecht, and B. D. Terris, "Magnetic recording at 1.5Pb m^2 using an integrated plasmonic antenna," Nat. Photonics **4**(7), 484–488 (2010).

19. N. Zhou, Y. Li, L. Traverso, and X. Xu, "Optical and thermal behaviors of plasmonic bowtie aperture and its NSOM characterization for heat-assisted magnetic recording," IEEE Trans. Magn. **52**(2), 1100105 (2016).

20. T. Matsumoto, K. Nakamura, T. Nishida, H. Hieda, A. Kikitsu, K. Naito, and T. Koda, "Thermally assisted magnetic recording on a bit-patterned medium by using a near-field optical head with a beaked metallic plate," Appl. Phys. Lett. **93**(3), 031108 (2008).

21. Y. Chen, J. Chen, X. Xu, and J. Chu, "Fabrication of bowtie aperture antennas for producing sub-20 nm optical spots," Opt. Express **23**(7), 9093–9099 (2015).

22. J. B. Leen, P. Hansen, Y.-T. Cheng, A. Gibby, and L. Hesselink, "Near-field optical data storage using C-apertures," Appl. Phys. Lett. **97**(7), 073111 (2010).

23. P. B. Johnson and R.-W. Christy, "Optical constants of the noble metals," Phys. Rev. B **6**(12), 4370–4379 (1972).

24. N. Zhou, Y. Li, and X. Xu, "Resolving near-field from high order signals of scattering near-field scanning optical microscopy," Opt. Express **22**(15), 18715–18723 (2014).

25. R. Esteban, R. Vogelgesang, and K. Kern, "Apertureless near-field optical microscopy: differences between heterodyne interferometric and non-interferometric images," Ultramicroscopy **111**(9-10), 1469–1474 (2011).

1. Introduction

Many efforts have been made towards confining optical energy into spots with sizes smaller than the optical diffraction limit. Recently, the use of the surface plasmon polaritons (SPPs) is one of the most studied ways of overcoming such the diffraction limit [1,2]. The collective oscillations of electrons in the boundary of a metal and a dielectric called surface plasmons can be generated with an incident wave on such a boundary. While oscillating at the same frequencies as the incident wave, plasmonic waves can have much shorter wavelengths. This provides a great means to concentrate electromagnetic energy to dimensions that are much smaller than the diffraction limit of light. Plasmonic devices are nanoscale structures with dimension comparable to the wavelength of the plasmonic oscillations. There have been studies on plasmonic devices for light focusing with different types of geometries including 1-dimensional boundaries between 2 dimensional metal-dielectric crystals [3], nanoparticles, slits, rods, wedges, rings, V-shaped grooves [4], and nano-diabolo [5], among others. Light focusing plasmonic devices have been widely used for many different applications including near-field scanning optical microscopy NSOM [6,7], photovoltaics, light emission [7], and nano-lithography [8].

Nanoscale ridge apertures fabricated in a metal film are amongst the most successful plasmonic devices for localization and enhancement of optical fields [9,10]. The gap between ridges efficiently confine far-field light irradiation into a nanoscale near field while the metal screen blocks far field illumination. It has been shown that the size of the localized spot is directly related to the size of the gap [11]. Due to their planar geometry, ridge apertures can be fabricated in large numbers on one substrate, which makes them suitable for parallel processing such as parallel near field optical lithography [12,13]. One of the most promising applications for nanoscale ridge apertures that has been investigated recently is for the development of plasmonic near field transducers (NFT) [14] for Heat Assisted Magnetic Recording (HAMR) [15]. Because of the inherent magnetic instability of small volumes when the bit size of a recording media reduces [16], conventional magnetic recording has reached the limit of miniaturization of about 1TB/in^2. For HAMR, media with higher stability is used, and an NFT creates a very localized intense electromagnetic field that heats up the medium thus decreases its coercivity. Among previously reported NFTs there were structures with different shapes including lollipops [17], E-shape structures [18], bowtie apertures [19], and nano beaks [20].

In the past, most of the ridge apertures were made using sequential fabrication methods such as focused ion beam (FIB) milling. These methods are relatively simple because they require a few steps only, for example, metal deposition and ion beam milling for FIB. One of the disadvantages of using FIB for fabrication is the proximity effect that produces rounded features and reduces the localization of light. Schemes to overcome this problem include

milling in such a way that the input side of light is the one with the FIB milled rounded feature and the exit side has a minimum rounded shape for light focusing [21,22].

This paper presents a novel method for fabricating ridge apertures using planar layer-by-layer lithography process. The apertures are constructed in the cross section of a dielectric layer surrounded by metal layers from top and bottom. This method can potentially overcome the proximity effect in the FIB process, and also be suitable for mass production of aperture arrays. Numerical computations are used for the design of these apertures. The fabricated apertures are characterized using scattering near field optical microscopy (s-NSOM).

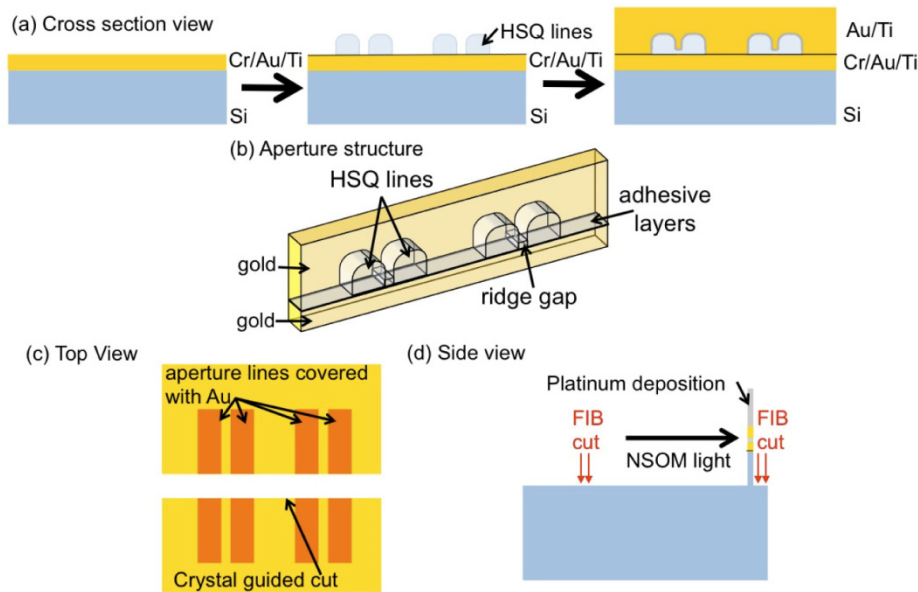## 2. Layer-by-layer fabrication of ridge apertures

Fig. 1. Schematic of the fabrication. (a) Cross section view of the process to create the aperture lines. (b) Schematic of the final aperture. (c) Top view of the substrate cutting process for s-NSOM measurements. (d) Side view of the thinning of the wall to create the apertures.

Figure 1(a) shows the procedure to fabricate the ridge aperture in a layer-by-layer manner. A cleaned silicon substrate is coated with layers of titanium, gold, and chrome. A 5 nm titanium layer serves as an adhesion layer between the 150 nm of gold and the silicon substrate, while a 3 nm chrome layer serves as an adhesion layer between the gold layer and a photo resist layer of hydrogen silsesquioxane (HSQ). HSQ was chosen for being a negative resist that would allow for the structure to maintain its shape and for being transparent which are needed for our purpose. The HSQ is coated at 4000 RPM for 45 seconds and soft baked at 120°C for 3 minutes, and then exposed using electron beam at a current of 0.3 nA with a dose of 2000 $\mu C/cm^2$. The exposure pattern of lines are shown in the second figure in Fig. 1(a). The exposed HSQ is further developed in tetramethylammonium hydroxide for 45 seconds. This process is intended for generating pairs of lines of HSQ with thickness of about 85 nm and a width of 220 nm, which can vary according to the design. The spacing between the lines in each pair is 25 nm. However there is residual HSQ left in between the HSQ lines due to the proximity effect during e-beam writing as shown in Fig. (1a). The amount of the residual is consistent as long as the substrate materials and exposure conditions remain the same. After developing HSQ, a 5 nm layer of titanium and 200 nm layer of gold are coated in a substrate rotation chamber to fill the ridge between the two lines of HSQ with gold. The final structure is illustrated in Fig. 1(b). It forms a previously studied c-aperture [22]. The gap is found to be about 40 nm from scanning electron microscopy (SEM) imaging, and this gap size produces a

satisfactory near-field according to numerical calculations and s-NSOM measurements described below.

Great efforts have been made in order to access the structure for NSOM measurement, as illustrated in Fig. 1(c) and described below. First a laser cut was made using an amplified femtosecond laser cutting system as shown in Fig. 1(c), along the silicon crystal lattice direction (the electron beam exposed lines are intentionally made perpendicular to the crystal lattice orientation). The laser does not directly cut the exposed lines to avoid damage to the fabricated aperture. The substrate is then broken apart by mechanical force. In order to access the aperture using an NSOM tip, a cross section wall is made using FIB milling close to the edge of the cut substrate as shown in Fig. 1(d). This relatively wide FIB milling (about 30 µm) allows light to reach the aperture. Before the FIB milling, a layer of platinum of about 6 µm thick is deposited as shown. This additional platinum layer on top of the aperture helps to block background light during NSOM measurements as well as to protect the apertures during the FIB milling. We fabricated a 6 µm tall platinum wall to avoid the interference of the scattered light around the wall with our NSOM measurements.

Figure 2 shows SEM images of intermediate steps including the exposure and development of the HSQ lines shown in Fig. 2(a) and the edge of the substrate after the laser cut shown in Fig. 2(b). Figure 2(c) shows a front view of 2 apertures after the entire sample preparation process for the s-NSOM measurement is finished.
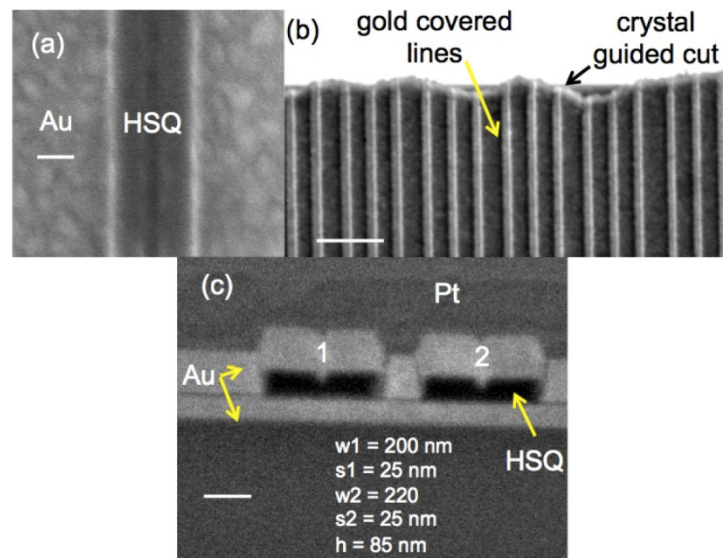

Fig. 2. SEM images of the structure during intermediate steps. (a) Exposed and developed HSQ lines (scale bar is 200nm). (b) Aperture lines on edge of the substrate after crystal guided cut (scale bar is 1 µm). (c) Zoomed cross section picture of 2 apertures (Inset scale bar is 200 nm).

3. Electromagnetic simulation

Full wave 3D simulations of the apertures were performed using ANSYS HFSS, a commercial FEM based electromagnetic equation solver. The aperture consists of two HSQ lines of width (w) 220 nm each. The height (h) of the HSQ lines was considered to be 85 nm. The spacing (s) between the two lines was 25nm. Gold reached into the spacing between the two lines to a distance d = 45 nm, resulting in a gap distance between the tip of the gold and the bottom gold layer of 40 nm. A fillet radius of 20 nm was used at the apex of the penetrated portion of the gold in order to resemble the fabricated geometry as observed from the SEM images. The thickness of the aperture was taken to be 100 nm and a Gaussian beam

of radius 500 nm, polarized along the vertical direction in the figure, was incident on the aperture. Absorption radiation boundary conditions were used at the outer surfaces of the model and the wavelength of 633 nm was used. Figure 3(a) shows the schematic of the model along with the key dimensions and the polarization of the incident beam. The optical properties of gold were taken from [23].
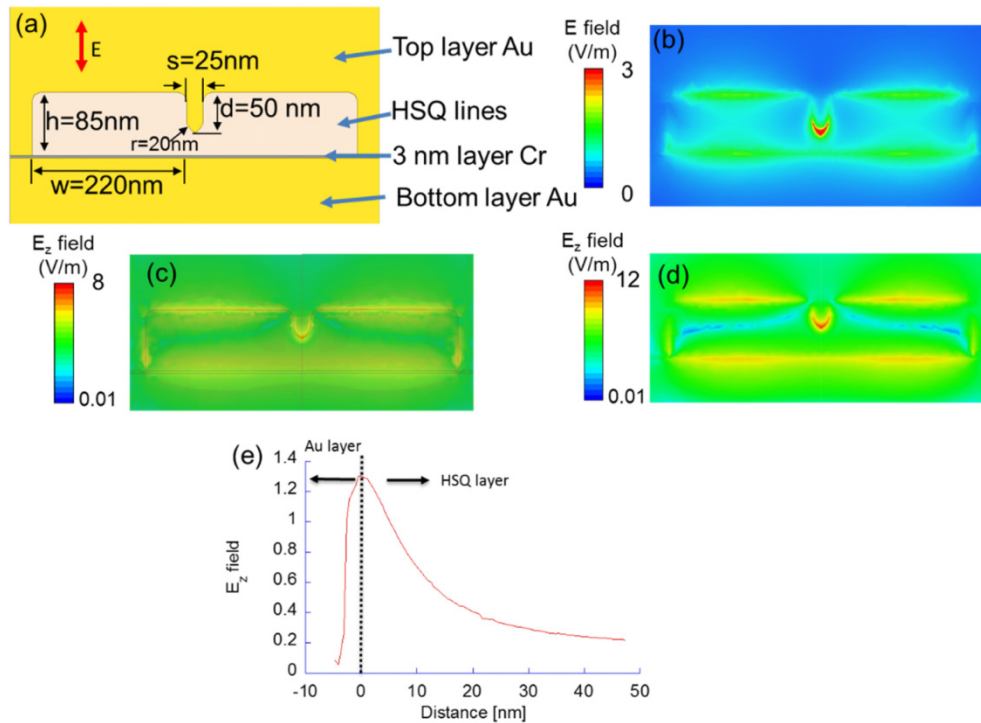

Fig. 3. (a) Electromagnetic simulation model for the cross sectional ridge waveguide apertures. (b) Electric field distribution taken 5nm above the exit plane of the apertures for the model depicted in (a). Electric field (z component) within the (c) metal layer and (d) HSQ layer. (c) and (d) are plotted in logarithmic scale for better clarity. (e) Decay of electric field within the HSQ and metal layer.

Figure 3(b) shows the electric field distribution corresponding to Fig. 3(a) at a distance of 5 nm from the aperture. The tip of the penetrated portion of the top layer of gold acts as a lightning rod and helps the confinement of electric field giving rise to an intense hot spot. Coupled with the effect of the localized surface plasmons, the electric field is enhanced by several times at the tip compared with the incident light. The field strength inside the HSQ layer and the metal layer is illustrated using the z component of the electric field. Figures 3(c) and (d) shows the z component of the electric field at a plane right above (1 nm above) the exit plane and at a plane 1nm below the exit plane. It can be seen that the maximum field strength within the HSQ layer is 12 times that of the incident field while the it only 8 times within the metal layer. The field generated due to the surface plasmons at the apex of the tip penetrate to different distances within the HSQ layer and the metal, and the skin depths obtained from Fig. 3e are 2.98 nm inside the metal layer and 16.1 nm inside the HSQ layer.

It is noted that the presence of a thin layer of titanium between the HSQ layer and the top gold layer could reduce the field strength at the tip and the simulation indicates that the field strength can decrease by a factor of up to 1.6. However, since the 5 nm nominal thickness of Ti might not be necessarily conformal, the effect of the Ti layer might not be as large as the simulation results. If detailed information about the Ti layer is known, it will be possible to

Research Article

Vol. 24, No. 23 | 14 Nov 2016 | OPTICS EXPRESS 26021

Optics EXPRESS

use the effective medium theory which employs an effective dielectric constant consisting of the volume fraction of Ti and Au in the Au/Ti layer to account for the effect of titanium.
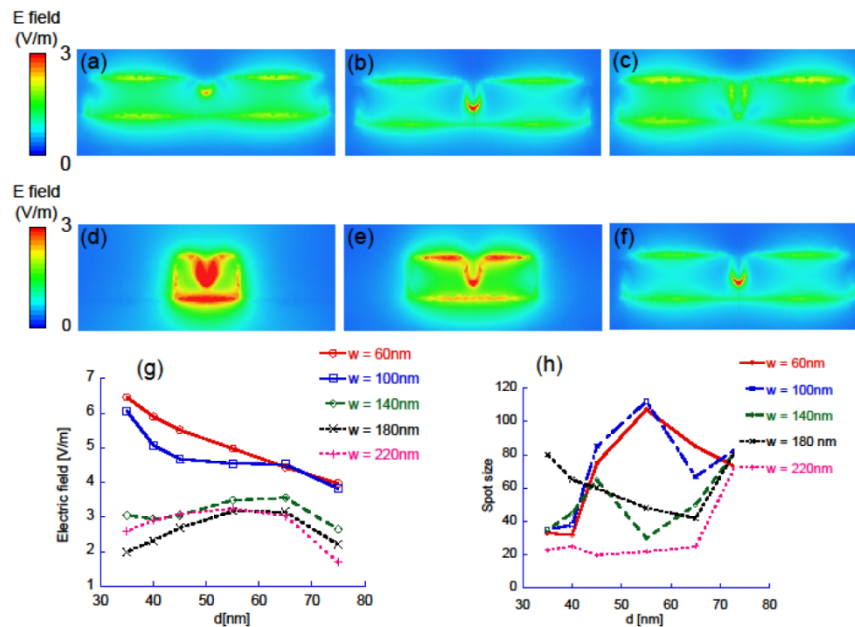

Fig. 4. Electric field distributions for (a) d = 20 nm, (b) d = 45 nm and (c) d = 75 nm when the other dimensions are fixed according to Fig. 3(a). Electric field distributions for (d) w = 40 nm, (e) w = 120 nm and (f) w = 220 nm when the other dimensions are fixed according to Fig. 3(a). (g) Electric field enhancement and (h) Spot size for varying values of w and d. The electric field distribution plots are taken 5nm above the exit plane of the apertures and the incident electric field was considered to be 1V/m.

As with any ridge apertures, the dimensions of the aperture play an important role in determining the functionality of the apertures and their ability to concentrate light into a hotspot. With respect to the fabricated apertures, the penetration depth and the width of the apertures are the two important parameters which affect how the apertures function and accordingly, we studied the simulated performance of the apertures when the penetration depth of the gold and the width of the individual HSQ lines are varied.

Figures 4(a)–4(c) show the electric field distribution at a plane 5 nm from the exit plane when the penetration depth, d is varied as 20 nm, 45 nm and 75 nm respectively. All other dimensions are kept constant as in Fig. 3(a). For a particular wavelength, the change in the penetration depth causes a change in the charge accumulation at the tip. We see that while there is no field localization for d = 20 nm or d = 75 nm in Figs. 4(a) and 4(c) respectively, there is a range of d, where the field concentration at the tip can be obtained when d is about 45 nm +/− 10 nm (only 45 nm is shown).

Next, we study the effect of the change in the aperture size by altering the HSQ line widths. In Figs. 4(d)-4(f), the line width, w is 40 nm, 120 nm and 220 nm respectively and all the other dimensions are fixed as in Fig. 3(a). From the results of the electric field, we find that changing the aperture width brings about a marked change in the charge accumulation due to surface plasmon at the edge of the gold-HSQ interface. In Fig. 4(d), when the line width is 40 nm, the field at the tip is several times than the incident field but at the same time there is a high field concentration at the interface between the bottom gold layer and HSQ lines which will prevent from realizing an isolated hot spot. When the line width is increased to 120 nm as in Fig. 4(e), the field concentration at the interface starts spreading out along the top and bottom gold-HSQ interface but an isolated spot at the tip is still not obtained.

Increasing the line width even further to 220 nm helps in isolating a hot spot as seen in Fig. 4(f). Extending the line width to large than 220 nm resulting in a nearly identical field as what is shown in Fig. 4(f).

In order to quantify the performance of the apertures, electric field 5 nm above the aperture and the spot size were evaluated for more values of w and d. Figure 4(g) shows the electric field when w and d are varied. It appears that a narrower width w will produce a higher field intensity. However, from the spot size for different values of w and d shown in Fig. 4(h), it can be seen that the spot size tends to become larger when w is smaller. This is due to the effect of the edge plasmon at the interface of the gold and the HSQ layer. Therefore the selection of the aperture sizes should consider both the field intensity and the spot size.

From these calculations and considerations of fabrication processes, we focus on the demonstration and characterization of apertures with w = 220 nm and d = 45 nm.

4. NSOM Characterization

The fabricated apertures were positioned in the s-NSOM system where far field images were first taken through an objective lens. Figure 5(a) shows far field image of the exit of the apertures when light is incident on them from behind. Light emerges from the expected area of the exit of the aperture. Figure 5(b) shows an illustration of the top view of the far field measurement including the necessary FIB cuts to thin down the wall to allow an incident light.
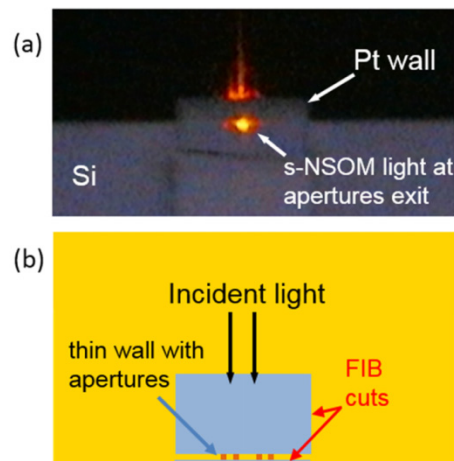

Fig. 5. Far-field images of apertures. a) Front view of a far field image. b) Top view of the schematic.

In order to characterize the optical near field of the fabricated apertures, an s-NSOM was used. A home built s-NSOM based on a commercial AFM system was used for this purpose. The s-NSOM was operated in transmission mode where light of wavelength 633 nm was focused on the sample with the help of an objective lens. At the same time, an AFM tip was engaged with the sample in the tapping mode and the sample was raster scanned. The scattered light from the AFM tip was then collected by a separate objective lens and was detected by a photodetector. The scattered light signal was demodulated with a lock-in amplifier at the tip oscillating frequency and its higher harmonics was used to extract the near field signal, which has reduced background noise. A detailed description of the experimental setup has been given elsewhere [24].
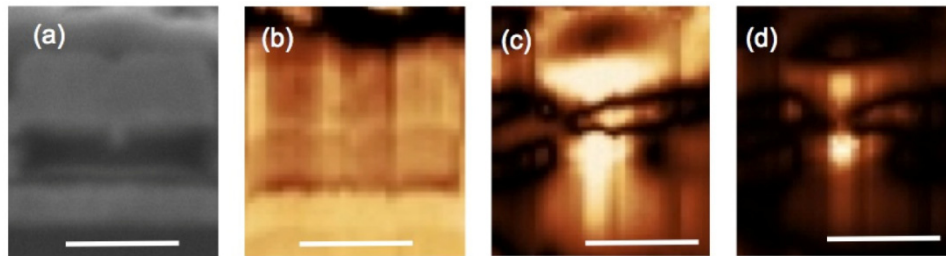
Fig. 6. Experimental characterization of the apertures. (a) SEM image of the aperture, (b) AFM topography of the aperture, (c) s-NSOM signal collected at the 2nd harmonic of the tip oscillation frequency from the aperture of (a) and (d) s-NSOM signal collected at the 3rd harmonic of the tip oscillation frequency from the aperture of (a). The scale bar in these figures is 250 nm.

Figure 6 shows the s-NSOM results as well as the SEM image and the AFM topography. Figure 6(a) shows the SEM image of an aperture fabricated according to dimension discussed in the previous section. Figure 6(b) shows the corresponding AFM topography image. It can be seen from the AFM topography image that the exposed surface of the cross section, unlike normal ridge apertures fabricated by methods such as FIB milling, is fairly planar. Figure 6(c) shows the s-NSOM signal collected at the 2nd harmonic of the tip oscillation frequency and Fig. 6(d) shows s-NSOM signal collected at the 3rd harmonic of the tip oscillation frequency. Both Figs. 6(c) and 6(d) show the enhancement of the field intensity at the tip of the gold protrusion (the upper bright spot is from the top of the gold film). However, it is seen that the high intensity spot from the third harmonic measurement is closer to what is predicted by the simulation shown in Fig. 3(b), Using low harmonic detection, the background from the AFM cantilever and surrounding regions makes it difficult to observe the true near field signal at sufficiently high resolution and unwanted background fringes appear the image in Fig. 6(c), which are commonly seen in s-NSOM measurements [24, 25]. Higher harmonic signals as seen in Fig. 6(d) provide a better background suppression and reduction of the peripheral fringes and helps in better visualization of the near field spot. From the NSOM measurements, the full width at half maxima of the near field spot is 72 nm x 76 nm. The simulated spot size at a distance of 5 nm from the exit plane is 22 nm x 28 nm, and decays to 32 nm x 45 nm at 10 nm from the exit plane and 77 nm x 77 nm at 20 nm from the exit plane. The measured value of the spot size is affected by the convolution between the tip radius of the AFM probe (~10 nm) and the actual spot. Additionally, the tip oscillates with an amplitude of about 20 nm during the NSOM measurements which can also make the spot size larger than that right above the exit plane

5. Conclusion

We demonstrated a concept of using a layer-by-layer fabrication process to produce ridge apertures in the cross section of layered thin films. Numerical calculations of the electric field distribution were used to evaluate the apertures. The s-NSOM measurements showed the localization of the exit field. Further development and refinement of the fabrication and characterization methods will allow fabrication of apertures in large quantities for many applications.

Funding